Novel one step preparation of silica supported Pd/Sr and Pd/Ba catalysts *via* an organometallic precursor: Application in hydrodechlorination and hydrogenation

Errun Ding[a], Satyakrishna Jujjuri[b], Matthew Sturgeon[a], Sheldon G. Shore[a], Mark A. Keane[c,*]

[a] *Department of Chemistry, The Ohio State University, Columbus, USA*
[b] *Department of Chemical and Materials Engineering, University of Kentucky, Lexington, USA*
[c] *Chemical Engineering, School of Engineering and Physical Sciences, Heriot-Watt University, Edinburgh EH14 4AS, Scotland, UK*

ABSTRACT

A gas phase hydrodechlorination (HDC) of chlorobenzene (CB) and 1,2-dichlorobenzene (1,2-DCB) has been examined over Pd/SiO_2 (prepared by impregnation with $Pd(C_2H_3O_2)_2$) and two alkaline earth metal (AEM = Sr and Ba) promoted Pd/SiO_2 catalysts prepared from the organometallic precursor $\{(DMF)_x AEMPd(CN)_4\}_\infty$ (AEM = Sr, Ba; $x = 4, 3$). While Sr/SiO_2 or Ba/SiO_2 exhibited no measurable HDC activity, the bimetallic catalysts delivered specific HDC rates (per Pd metal surface area) that were up to a factor of 20 times higher than that recorded for Pd/SiO_2. The initial fractional dechlorination recorded for $Sr–Pd/SiO_2$ and $Ba–Pd/SiO_2$ was up to two orders of magnitude greater than that for Pd/SiO_2. We associate this promotional effect with a surface Pd/AEM synergy that enhances Pd dispersion with a resultant increase in H_2 chemisorption capacity allied to a more effective C–Cl bond activation for hydrogen scission. Bulk and surface catalyst characteristics, pre-and post-reaction, have been probed by IR, BET, TPR, H_2 chemisorption/TPD, XRD, XPS and TEM-EDX analyses. While 1,2-DCB conversion over Pd/SiO_2 was lower than that observed for CB due to inhibitory inductive and steric effects, CB and DCB reactivity were comparable over $AEM-Pd/SiO_2$. Each catalyst exhibited a temporal decline in HDC performance that we link to deleterious Cl interactions which impact H_2 uptake/release capacity. Although the bimetallic catalysts were less susceptible to deactivation, the samples post-HDC retain an appreciable Cl content with a redispersion of both AEM and Pd components and a disruption to the surface electronic characteristics that is apparent from the XPS profiles. The presence of AEM had no effect on benzene hydrogenation performance over freshly activated samples but post-HDC, Pd/SiO_2 exhibited depleted hydrogenation activity whereas both bimetallics (notably $Sr–Pd/SiO_2$) generated a significantly enhanced hydrogenation response that we ascribe to a surface restructuring that is beneficial for aromatic reduction.

© 2008 Elsevier B.V. All rights reserved.

1. Introduction

Chloroaromatics are well established as persistent toxic compounds for which the environment has little assimilative capacity [1,2]. The introduction of stringent legislation has served to curtail those emissions from commercial operations that lead to contamination of water, land and air [3]. In addition to the legislative demands, the economic pressures faced by the commercial sector in the 21st century include loss of potentially valuable resources through waste, escalating disposal charges and increasing raw material/energy costs. Chlorobenzenes are commercially important, serving as end products and intermediates in the manufacture of herbicides, dyes and plant growth regulators [4]. Aromatic chlorination reactions are notoriously non-selective with limited control

over the ultimate product composition. The development of a low waste process that produces organo-halogen products necessitates the inclusion of a robust waste processing/detoxification component, where the energy requirements of such a down-stream process must be weighed against the possibility of raw material recycle. Catalytic hydrodechlorination (HDC) is an emerging "green" chloro-waste treatment that involves H_2 cleavage of one or more C–Cl bonds, lowering toxicity and generating reusable raw material. Based on three comprehensive reviews of the literature on hydrodehalogenation [5–7], it is clear that Pd is the most active dechlorination metal. Indeed, supported Pd has been demonstrated to be effective in chloroarene hydrodechlorination under ambient conditions [8–11]. In recent reports [8–10] we established that lanthanides (La, Ce, Sm, Eu, Gd and Yb), while HDC inactive, served to elevate appreciably the HDC activity of silica supported Pd. The promotional effect of lanthanide addition was not limited to HDC (hydrogenolysis) reactions but also extended to aromatic hydrogenation [12,13]. We examined the action of the

lanthanide when incorporated in a stepwise fashion pre- and post the inclusion of Pd [13] as well as the simultaneous addition of both Pd and the lanthanide (Ln) from the organometallic precursor $\{(DMF)_{10}Ln_2[Pd(CN)_4]_3\}_\infty$ [12–14]. We have now taken this work further by considering the HDC and hydrogenation performance of silica supported Pd/alkaline earth metal (AEM = Sr and Ba) bimetallics prepared from an analogous organometallic precursor, i.e. $\{(DMF)_x AEMPd(CN)_4\}_\infty$ (AEM = Sr, Ba; x = 4, 3).

The higher HDC activities delivered by Ln–Pd/SiO$_2$ were attributed principally to a surface Ln/Pd synergism involving H$_2$ transfer from Ln dihydride to the active Pd sites [13,14]. Alkaline earth metals can also form dihydrides which led Wright and Weller in an early series of studies [15] to propose a possible promotional effect in tandem with transition metals (such as Ni and Pt) in hydrogenation-dehydrogenation reactions. Indeed, alkaline earth metals have been used as Pd promoters in CO hydrogenation to produce methanol [16], acting to stabilize formate ion intermediates where Pd serves to dissociate H$_2$ [17]. The involvement of Sr or Ba in the development of HDC catalysts has not been addressed to any significant degree in the literature. It is, however, worth flagging the work of Simagina et al. [18] who made use of chemically bound H$_2$, in the form of MgH$_2$, to promote chlorobenzene HDC over Pd/C. Shekhar et al. [19] considered a related system in their study of CCl$_2$F$_2$ hydrogenolysis over Pd supported on a "carbon covered alumina" where the incorporation of Ba (by impregnation with Ba(NO$_3$)$_2$) had little effect on activity/selectivity but enhanced catalyst stability, minimizing deactivation and possibly limiting Pd sintering. Indeed, metal catalyst deactivation is a feature of gas phase HDC [5,20–23] as a result of HCl interaction(s) that poison(s) the active metal [5,21,24–26]. It is accepted that catalytic HDC, in common with most hydrogenolysis reactions, exhibits structure sensitivity [27] where the electronic structure of the active metal sites governs catalyst performance [28]. Coq and Figueras have noted that bimetallic Pd catalysts deliver elevated HDC activities relative to the corresponding monometallic when the second metal serves as an electron donor [29]. The charge transfer capabilities of AEM dopants have been demonstrated elsewhere for supported Pd and Ni systems with a significant impact on hydrogenation activity and selectivity [30]. In this study, we probe the possible contribution of surface hydride and/or electron donation in terms of mono- and di-chlorobenzene HDC and benzene hydrogenation over Sr–Pd/SiO$_2$ and Ba–Pd/SiO$_2$, providing catalyst characterization results pre- and post-reaction that are based on IR, BET, TPR, H$_2$ chemisorption/TPD, XRD, TEM and XPS analyses.

2. Experimental

2.1. Catalyst preparation, activation and characterization

The AEM-Pd complex $\{(DMF)_x AEMPd(CN)_4\}_\infty$, which served as the bimetallic catalyst precursor was prepared using a procedure similar to one previously described by Shore and co-workers (where the lanthanide salt was replaced by an alkaline earth metal salt) [31]. The associated crystal structures of the Ba–Pd and Sr–Pd precursors are shown in Fig. 1a and b, respectively, where the extended array and cyanide bridge linking Ba–Pd (2-D sheet structure) and Sr–Pd (1-D ladder array) are evident. The preparation of Ba–Pd/SiO$_2$ and Sr–Pd/SiO$_2$ followed a similar procedure. A solution of the bimetallic precursor in DMF (dimethyl formamide) was contacted with fumed SiO$_2$ to deliver a 5% w/w Pd loading; Pd/AEM = 1/1 mol/mol. The DMF was removed from the metal impregnated SiO$_2$ via dynamic vacuum over a period of 12 h at room temperature. IR spectroscopy was conducted on the impregnated samples using a Bruker Tensor 27 spectrometer: 32 scans at a resolution of 2 cm^{-1}. Nujol mulls of the impregnated sam-
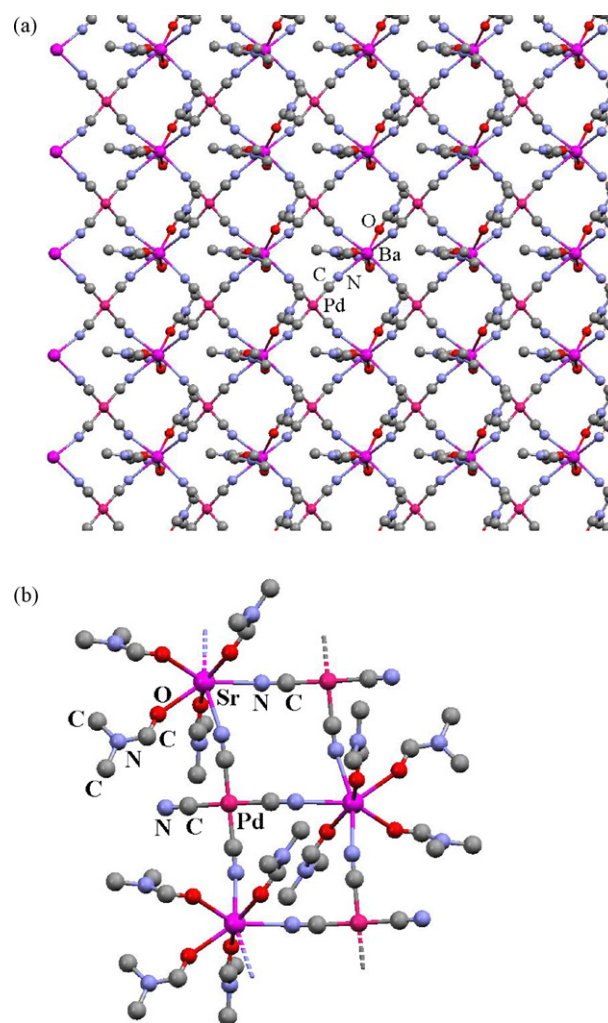

Fig. 1. The crystal structure of the organometallic catalyst precursors: (a) $\{(DMF)_3BaPd(CN)_4\}_\infty$ and (b) $\{(DMF)_4SrPd(CN)_4\}_\infty$.

ples were prepared in a dry box under an N$_2$ atmosphere using mineral oil (used as received from Aldrich). The resultant spectra were compared to their crystalline precursors; see Fig. 2I and II. Equivalent IR signals in the CN stretching region confirmed that the extended structures of the precursors were retained upon loading. The resulting white solid was removed in air and placed (in a quartz boat) in a furnace and flushed with H$_2$ (5% v/v in N$_2$) for 10 min and reduced under a constant H$_2$ flow at a heating rate of 10 K min^{-1} to a final temperature of 523 K, which was maintained for 30 min. The sample was then flushed in He and passivated in a 1% v/v O$_2$ (in He) flow at room temperature. A monometallic 5% w/w Pd/SiO$_2$ was prepared by contacting the same SiO$_2$ substrate with the acetate precursor (in DMF) with subsequent activation/passivation as above; details are provided elsewhere [32]. Sr/SiO$_2$ and Ba/SiO$_2$ were prepared by charging known amounts of SiO$_2$ and Sr (or Ba) powder into a reaction flask (located in a dry box) with vacuum transfer of liquid ammonia into the flask at 195 K. The mixture was kept under constant agitation for 3 h at which point the liquid ammonia was pumped away. Each sample was sieved (ATM fine test sieves) into a batch of 75 μm average particle diameter and subjected to a second reduction step (prior to catalysis) in a fixed bed tubular glass reactor (i.d. = 1.25 cm) by heating (10 K min^{-1}) in a 60 cm^3 min^{-1} stream of dry H$_2$ (99.999%) to a final temperature of 573 K that was maintained for 12 h.
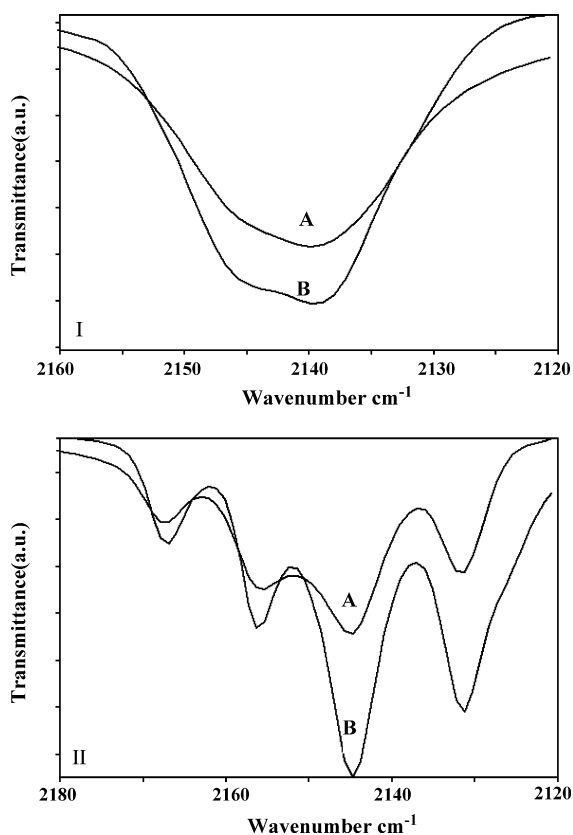
Fig. 2. IR spectra showing the cyanide stretching region: **I**, (A) {(DMF)$_3$BaPd(CN)$_4$}$_\infty$ supported on SiO$_2$ (Nujol mull) and (B) crystalline {(DMF)$_3$BaPd(CN)$_4$}$_\infty$ (KBr press); **II**, (A) crystalline {(DMF)$_4$SrPd(CN)$_4$}$_\infty$ (KBr press) and (B) {(DMF)$_4$SrPd(CN)$_4$}$_\infty$ supported on SiO$_2$ (Nujol mull).

BET surface area, temperature programmed reduction (TPR), H$_2$ chemisorption and temperature programmed desorption (TPD) were determined using the commercial CHEM-BET 3000 (Quantachrome) unit. The samples (0.05–0.1 g) were loaded in a U-shaped Quartz cell (21 cm × 3.76 mm i.d.). The total surface area was recorded in a 30% v/v N$_2$/He flow; pure N$_2$ (99.9%) served as the internal standard. After outgas for 30 min, at least two cycles of N$_2$ adsorption–desorption in the flow mode were employed using the standard single point BET method. TPR was performed in 20 cm^3 min^{-1} (Brooks mass flow controller) 5% v/v H$_2$/N$_2$ to 573 K at 10 K min^{-1} and the effluent gas passed through a liquid N$_2$ trap; changes to the carrier gas composition were monitored by a thermal conductivity detector (TCD) with data acquisition/manipulation using the TPR Win^{TM} software. The samples were swept with 20 cm^3 min^{-1} dry N$_2$ for 1 h at 573 K, cooled to room temperature and subjected to H$_2$ chemisorption using a pulse (50 μl) titration procedure. Any possible contribution due to β-palladium hydride formation was avoided as the H$_2$ partial pressure <2 Torr, well below the pressure (>11 Torr) required to generate the hydride [33]. The sample was thoroughly flushed with pure N$_2$ (20 cm^3 min^{-1}) for 30 min to remove any weakly bound H$_2$ and TPD conducted in the N$_2$ flow at 50 K min^{-1} up to 1273 K with a final isothermal hold of 15 min. Based on TCD calibrations and analysis of the effluent gas using a MICROMASS PC Residual Gas Analyser, the TPD profiles recorded in this paper can be attributed solely to H$_2$ release. BET surface area and H$_2$ uptake values were reproducible to within ±5% and the values quoted are the mean.

Transmission electron microscopy analysis was conducted using a JEOL-2000 TEM/STEM microscope equipped with a UTW energy dispersive X-ray (EDX) detector (Oxford Instruments) and operated at an accelerating voltage of 200 kV. The specimens were prepared by ultrasonic dispersion in 2-butanol, evaporating a drop of the resultant suspension onto a holey carbon support grid. The mean Pd particle sizes are quoted in this paper as surface area-weighted diameters ($\bar{d}_s$)

$$\bar{d}_s = \frac{\sum_i n_i d_i^3}{\sum_i n_i d_i^2} \qquad (1)$$

where n_i is the number of particles of diameter d_i. The TEM-EDX elemental composition was accurate to within ±0.1 atom %. X-ray powder data were collected on a Bruker D8 Advance X-ray powder diffractometer (Cu Kα radiation) from samples (subjected to a reductive atmosphere at 573 K) loaded in 0.5 mm Lindeman glass capillaries in a glove box and sealed. X-ray photoelectron spectroscopic (XPS) analyses were conducted using a Kratos Axis Ultra spectrometer with monochromatized Mg Kα radiation (1253.6 eV). A sample of activated/passivated catalyst was adhered to conducting carbon tape, mounted in the sample holder and subjected to UHV conditions ($\sim$10^{-9} Torr) overnight prior to analysis. Full range surveys (0–1000 eV) and high-resolution spectra (range of $\sim$30 eV) of Pd 3d$_{3/2}$/3d$_{5/2}$, Sr 3d$_{5/2}$, Ba 3d$_{5/2}$, Si 2p, O 1s, Cl 2p$_{3/2}$ and C 1s were collected; a physical mixture of PdCl$_2$ + SiO$_2$ served as a reference sample. The C 1s peak, centred at 284.5 eV was used as reference to calibrate the binding energy values. The signals for Pd, Sr, Ba and Cl were much weaker than Si and O, due to the low concentrations in the SiO$_2$ matrix with the result that extended scans were employed to improve the signal/noise ratio.

2.2. Catalytic system

The reactions were conducted *in situ* (after catalyst activation) with a co-current flow of the aromatic feed in H$_2$ (P_{H_2} = 092 atm). The reactor/procedure has been described in some detail elsewhere [34,35] but features pertinent to this study are given below. A layer of glass beads above the catalyst bed ensured that the reactants were vaporized and reached reaction temperature before contacting the catalyst. A Model 100 (kd Scientific) microprocessor controlled infusion pump was used to deliver the aromatic feed, *via* a glass/teflon air-tight syringe and teflon line at a fixed calibrated flow rate. All the HDC reactions were carried out at 423 K where isothermal operation was ensured by diluting the catalyst bed with ground glass (75 μm). CB (Aldrich, 99.9% v/v), 1,2-DCB (Aldrich, 99% v/v) and methanol solvent (Merck, 99.8% v/v) were used without further purification. The HDC reaction was monitored at an inlet hourly Cl/Pd mole ratio = 5 × 10^3 and a contact time = 0.02 min. In a series of blank tests, passage of each reactant in a stream of H$_2$ through the empty reactor, i.e. in the absence of catalyst, did not result in any detectable conversion. The reactor effluent was frozen in a liquid nitrogen trap for subsequent analysis which was made using a Perkin–Elmer Auto System XL chromatograph equipped with a split/splitless injector and a flame ionization detector, employing a DB-1 50 m × 0.20 mm i.d., 0.33 μm capillary column (J&W Scientific). The overall level of HDC was converted to mol % conversion using detailed calibration plots for each feedstock. Quantitative analysis was based on relative peak area with acetone as solvent where analytical repeatability was better than ±1% and the detection limit typically corresponded to a feedstock conversion less than 0.1 mol %. HDC performance is quantified in terms of fractional dechlorination (x_{Cl})

$$x_{Cl} = \frac{[Cl_{org}]_{in} - [Cl_{org}]_{out}}{[Cl_{org}]_{in}} \qquad (2)$$

where [Cl$_{org}$] represents concentration (mol dm^{-3}) of chlorine associated with the aromatic feed; *in* and *out* refer to the inlet

Table 1a

Palladium particle size from H_2 chemisorption uptake and XRD analysis, surface area weighted ($\bar{d}_s$) Pd particle size and metal particle (AEM and/or Pd) size range from TEM-EDX, pre- and post-HDC

	Pre-HDC (nm)				Post-HDC (nm)			
	H_2 chem.	TEM		XRD	H_2 chem.	TEM		XRD
		$\bar{d}_s$	Pd + AEM size range	Pd size		$\bar{d}_s$	Pd + AEM size range	Pd size
Pd/SiO$_2$	40	42[a]	<2–50[a]	33	71	63[a]	<5–100[a]	42
Sr-Pd/SiO$_2$	6	8[a]	<2–70[b]	7	26	19[a]	<2–70[b]	10
Ba-Pd/SiO$_2$	6	12[a]	<2–90[c]	9	26	30[a]	<2–80[c]	17

[a] Mean particle size/size range refers to Pd.

[b] Size range applies to both Pd and Sr.

[c] Size range applies to both Pd and Ba.

and outlet reactor streams, respectively. It has been demonstrated previously [36,37] that HCl is the only inorganic product with no detectable Cl_2 production, i.e. $[Cl_{org}]_{in} - [Cl_{org}]_{out} = [HCl]_{out}$. A chlorine mass balance (in the form of HCl product) was performed by passing the effluent gas through an aqueous NaOH trap $(3.5-8.0 \times 10^{-3}\,mol\,dm^{-3}$, kept under constant agitation at $\geq 300\,rpm)$ and monitoring continuously the pH change by means of a Hanna HI Programmable Printing pH Bench-Meter. The concentration of HCl generated was also measured by titrimetric analysis of the NaOH trap solution using a Metrohm (Model 728) Autotitrator ($AgNO_3$, combined Ag electrode); Cl mass balance was complete to better than ±10%. The percentage selectivity with respect to chlorobenzene (S_{CB} %) from the DCB feed is given by

$$S_{CB}\% = \frac{[CB]_{out}}{[DCB]_{in} - [DCB]_{out}} \times 100 \qquad (3)$$

Hydrogenation activity was also monitored by examining the reduction of benzene (as feed) at 423 K: inlet hourly benzene/Pd mole ratio = 35. The catalyst was activated as above, benzene conversion was monitored for 3 h on-stream, the catalyst was then contacted with 0.3 moles 1,2-DCB and the benzene feed was reintroduced with product analysis; cyclohexane was the only product detected. The percentage yield of cyclohexane ($Y_{cyclohexane}$ %) is defined as

$$Y_{cyclohexane}\% = \frac{[cyclohexane]_{out}}{[benzene]_{in}} \times 100 \qquad (4)$$

Repeated reactions with different samples from the same batch of catalyst delivered raw data reproducibility that was better than ±5%.

3. Results and discussion

3.1. Catalyst characterization

3.1.1. TEM/XRD/XPS

Exhaustive TEM analysis of Sr/SiO$_2$ and Ba/SiO$_2$ did not reveal any distinct metal particles but EDX mapping over areas up to $3 \times 10^5\,nm^2$ recorded appreciable surface Sr and Ba (up to 1 atom %) which is close to the bulk content, suggesting a well dispersed AEM phase. TEM examination of Pd/SiO$_2$ did show discrete Pd particles with a spherical morphology, as noted elsewhere [32,38]. Repeated and comprehensive TEM-EDX mapping of Sr–Pd/SiO$_2$ and Ba–Pd/SiO$_2$ demonstrated that both catalysts possess similar surface structure, i.e. presence of well dispersed Pd with larger Sr and Ba particles that exhibit a broad size range distribution. The average Pd particle sizes and particle size range (Pd and Pd + AEM) associated with the three catalysts pre-HDC are given in (Table 1a). A representative TEM image of Ba–Pd/SiO$_2$ is shown in Fig. 3 where the encircled regions "a" and "b" correspond to larger Ba particles with limited Pd content while regions "c" and "d" depict Pd particle
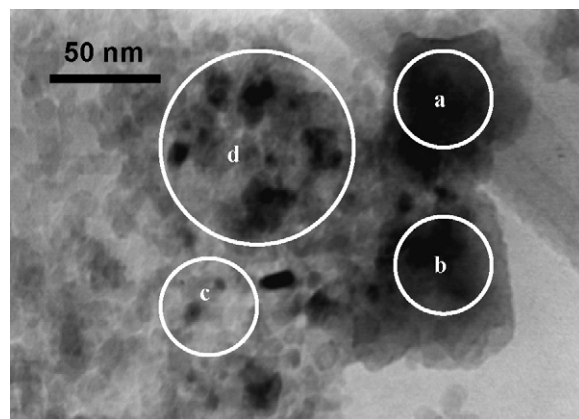
Fig. 3. Representative TEM image of Ba–Pd/SiO$_2$ (pre-HDC) with four encircled areas that were subjected to EDX analysis: see Table 1b for the resultant elemental composition.

rich regions relative to Ba; the corresponding elemental compositions are recorded in (Table 1b). Repeated TEM–EDX mapping (areas 1000–6000 nm^2) of Ba–Pd/SiO$_2$ delivered a wide range of Ba/Pd surface ratios (34-0.1), a response that also characterized the pre-HDC Sr–Pd/SiO$_2$ (28-0.1), suggesting an appreciable surface composition heterogeneity. On the basis of the TEM-EDX analyses, we can state that the AEM particles/clusters in the bimetallics were larger than 15 nm (and up to 90 nm) while the largest Pd particle detected was 20 nm. The surface weighted mean Pd size was significantly lower for the bimetallic samples (see Table 1a); Pd/SiO$_2$ contained Pd particles up to 50 nm in diameter. These results suggest that the incorporation of an AEM component, albeit from an unconventional source, serves to enhance Pd dispersion (at the same Pd loading) when compared with a conventional Pd/SiO$_2$ preparation.

Table 1b

Representative elemental composition from TEM-EDX for (see Fig. 3) Ba-Pd/SiO$_2$ pre-HDC and for (see Fig. 12) Sr-Pd/SiO$_2$ post-HDC

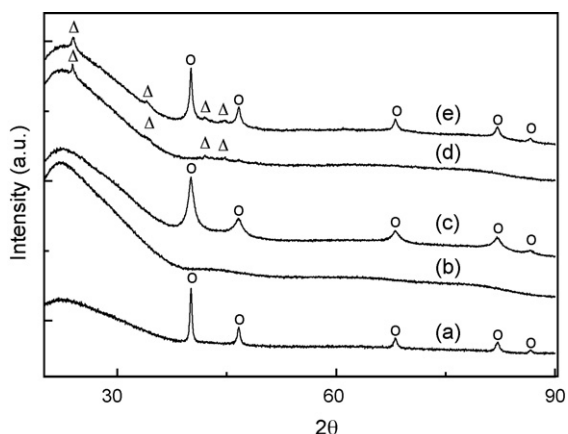| Ba–Pd/SiO$_2$	Elemental Composition from TEM-EDX (atom %)				
	Ba	Pd	Si	O	Cl
Pre-HDC					
Region (a)	20.2	0.6	12.3	66.9	–
Region (b)	7.1	0.8	29.4	62.7	–
Region (c)	<0.1	1.5	41.6	56.8	–
Region (d)	0.5	6.4	35.8	57.2	–
Sr–Pd/SiO$_2$	Sr	Pd	Si	O	Cl
Post-HDC					
Region (a)	0.7	54.1	13.9	29.0	2.3
Region (b)	0.8	32.8	25.8	39.0	1.6
Region (c)	0.2	«0.1	39.3	60.1	0.4

Fig. 4. XRD patterns for the activated catalysts (pre-HDC): (a) Pd/SiO$_2$, (b) Sr/SiO$_2$, (c) Sr–Pd/SiO$_2$, (d) Ba/SiO$_2$, (e) Ba–Pd/SiO$_2$. Note: **O** indicates peak assignment for *fcc* Pd and △ for BaSiO$_3$ phases.

The X-ray diffraction patterns given in Fig. 4 provide important bulk structural characteristics for the activated catalysts. The pattern associated with Pd/SiO$_2$ is consistent with an exclusive cubic geometry with the five peaks (see profile (a)) at $2\theta = 40.1^\circ$, 46.7°, 68.1°, 82.15° and 86.61° corresponding (from the JCPDS standards [39]), respectively, to (1 1 1), (2 0 0), (2 2 0), (3 1 1) and (2 2 2) Pd planes. The XRD pattern for Sr/SiO$_2$ is featureless while there is some evidence of bulk BaSiO$_3$ in the Ba/SiO$_2$ sample, although the signals are very weak. There was no detectable bulk AEM hydride phase in our samples on the basis of the XRD analysis but this does not rule out the possibility of a well dispersed phase as is suggested by the TEM-EDX analysis. However, Fokin et al. [40,41] have reported that higher H$_2$ pressures (0.5–3.0 MPa at 423–473 K) are required for AEM hydride formation. We can not discount the possible involvement of surface Pd to facilitate AEM hydride formation through a surface synergism involving dissociative H$_2$ adsorption on Pd sites with subsequent H transfer to the AEM component. The Sr–Pd/SiO$_2$ sample only exhibited reflections that are characteristic of metallic Pd while the XRD pattern recorded for Ba–Pd/SiO$_2$ is consistent with the presence of cubic Pd and a BaSiO$_3$ phase. The average Pd particle size obtained from standard XRD line broadening analysis is given in Table 1a where, in agreement with TEM analysis, Pd particle size in the bimetallics is smaller when compared with Pd/SiO$_2$ There was no evidence, on the basis of XRD analysis, of any bulk "alloy" formation in the two bimetallic catalysts. Likewise, Shekar et al. [19] did not observe any alloying in their Ba–Pd/carbon covered alumina catalyst.

XPS analysis can give some insight into metal interactions at the surface and the XPS profiles for the passivated unused samples over the Pd and AEM binding energy regions are presented in Fig. 5; the associated binding energies and surface elemental ratios are recorded in Table 2. The XPS profile generated for Pd/SiO$_2$ (profile (a) in Fig. 5I) exhibits two peaks where the associated Pd 3d$_{5/2}$ binding energy is in good agreement with that recorded in the literature [42,43]. The (principal) Pd 3d$_{5/2}$ signal was shifted by 0.5 eV to a lower binding energy in the bimetallic systems, a response that can be attributed to electron donation from the electropositive AEM. The appearance of an indistinct shoulder to the principal peak may be attributed to residual Pd oxide and is similar to the signal recorded (at 336.7 eV) for bulk PdO by Suhonen et al. [44]. The AEM binding energies recorded in Table 2 are close to the 3d$_{5/2}$ values reported in the literature for Sr^{2+} (132.2 eV) and Ba^{2+} (778.3 eV) [45]. The peaks corresponding to
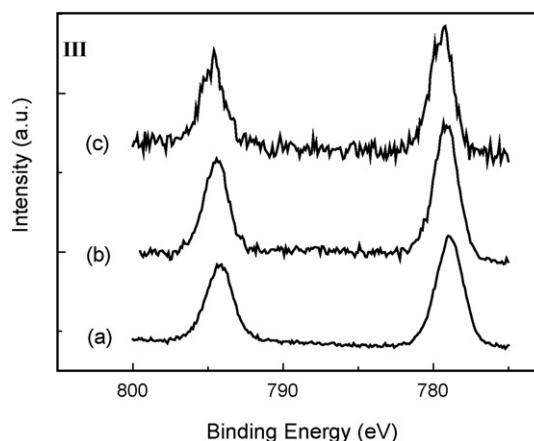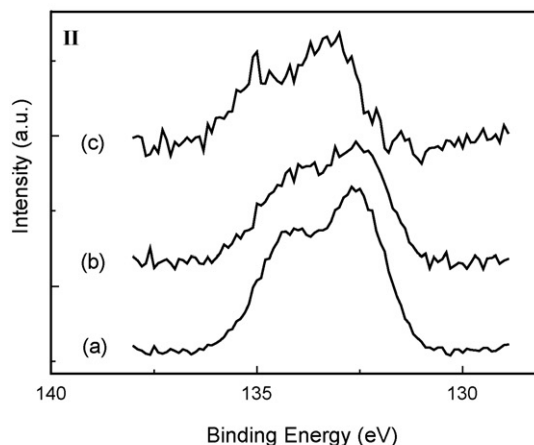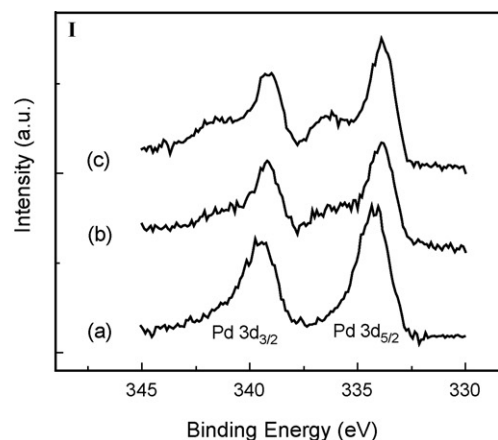

Fig. 5. XPS profiles for the passivated catalysts: **I** over the Pd 3d region for (a) Pd/SiO$_2$, (b) Sr–Pd/SiO$_2$ and (c) Ba–Pd/SiO$_2$ (all pre-HDC); **II** over the Sr 3d region for (a) Sr/SiO$_2$ (pre-HDC), (b) Sr–Pd/SiO$_2$ (pre-HDC) and (c) Sr–Pd/SiO$_2$ (post-HDC); **III** over the Ba 3d region for (a) Ba/SiO$_2$ (pre-HDC), (b) Ba–Pd/SiO$_2$ (pre-HDC) and (c) Ba–Pd/SiO$_2$ (post-HDC).

AEM 3d$_{5/2}$ in AEM-Pd/SiO$_2$ were shifted by 0.1–0.3 eV compared with AEM/SiO$_2$; see Fig. 5II and III for the Sr 3d$_{5/2}$ and Ba 3d$_{5/2}$ responses, respectively. XPS analysis generated AEM/Pd surface atom ratios (see Table 2) that were very close to those obtained by TEM–EDX at lower magnification (corresponding to mapped areas = 3×10^5 nm^2), i.e. 1.4 for Sr–Pd/SiO$_2$ and 0.6 for Ba–Pd/SiO$_2$, demonstrating a greater relative surface enrichment by the Sr component.

Table 2
Pd, Sr, Ba and Cl binding energies (principal peaks given in bold) and atomic ratios from XPS analysis of passivated catalysts, pre- and post-HDC; XPS characteristics of a model $PdCl_2 + SiO_2$ mixture are also included

Catalyst	Pre-HDC			Post-HDC					
	Binding energy (eV)		Atomic ratio	Binding energy			Atomic ratio		
	Pd $3d_{5/2}$	AEM $3d_{5/2}$	AEM/Pd	Pd $3d_{5/2}$	AEM $3d_{5/2}$	Cl $2p_{3/2}$	AEM/Pd	Cl/Pd	Cl/(AEM + Pd)
Pd/SiO$_2$	**334.3**	–	–	**334.3**	–	–	–	«0.1	–
Sr/SiO$_2$	–	132.5	–	–	–	–	–	–	–
Ba/SiO$_2$	–	778.9	–	–	–	–	–	–	–
Sr–Pd/SiO$_2$	**333.8** 335.8[a]	132.6	1.8	**334.4** 336.5[b]	133.2	197.6	1.7	2.3	0.9
Ba–Pd/SiO$_2$	**333.8** 336.0[a]	779.2	0.8	**334.2** –[c]	779.6	197.2	1.6	4.4	1.7
		Binding energy (eV)							Atomic ratio
		Pd $3d_{5/2}$			Cl $2p_{3/2}$				Cl/Pd
PdCl$_2$ + SiO$_2$		334.4 336.2			196.9				1.6

[a] Shoulder to the principal peak.
[b] Pd $3d_{5/2}$ peak splitting.
[c] Peak splitting not apparent in this sample but total peak width is close to that recorded for Sr–Pd/SiO$_2$ (post-HDC) and PdCl$_2$ + SiO$_2$.

3.1.2. BET/TPR

The BET surface areas are presented in Table 3a where the value quoted for Pd/SiO$_2$ is close to that of the SiO$_2$ support (200 m^2 g^{-1}) whereas the supported bimetallics exhibited appreciably lower areas. This was also the case for the supported AEM samples, i.e. 145 and 149 m^2 g^{-1} for Sr/SiO$_2$ and Ba/SiO$_2$, respectively. This loss of area can be ascribed to pore blocking (pore volume of SiO$_2$ = 1.5 cm^3 g^{-1}) by the AEM component, which is consistent with a high degree of dispersion of the supported AEM phase. It should be noted that a similar drop in area was observed in the analogous preparation of SiO$_2$ supported lanthanides [12–14]. The temperature programmed reduction (TPR) profiles for the passivated SiO$_2$ supported Pd, Sr–Pd and Ba–Pd samples are recorded in Fig. 6; TPR of Sr/SiO$_2$ and Ba/SiO$_2$ up to 573 K (not shown) were featureless. The profile for Pd/SiO$_2$ is dominated by a negative peak at 371 K representing H$_2$ release and can be attributed to the decomposition of β-Pd hydride that can form at room temperature in the presence of H$_2$ [42,46–51]. The absence of any obvious H$_2$ consumption during the temperature ramp prior to the observed H$_2$ release suggests the presence of zero valent Pd before commencement of Pd/SiO$_2$ TPR. Indeed, a room temperature reduction of PdO has been reported in the literature [46–48]. An ill-defined H$_2$ consumption at the final isothermal hold (573 K) is in evidence that is indicative of a temperature induced reduction step, a response that has also been reported elsewhere [52,53] and may be attributed to metal/support interactions that stabilise surface Pd oxide. The bimetallic samples also exhibited a negative TPR peak at 368 ± 2 K (Fig. 6); peak integration yielded the molar H/Pd ratios recorded in Table 3a. The H/Pd value (0.34) obtained for Pd/SiO$_2$ is in accord with the literature [50,54] while both bimetallics delivered an appreciably lower value (0.19), which suggests an inhibition of Pd hydride formation. Low H/Pd ratios have been noted elsewhere and linked to a metal redispersion leading to smaller Pd size [50] while a complete suppression is associated with alloy formation [55]. Our TEM analysis
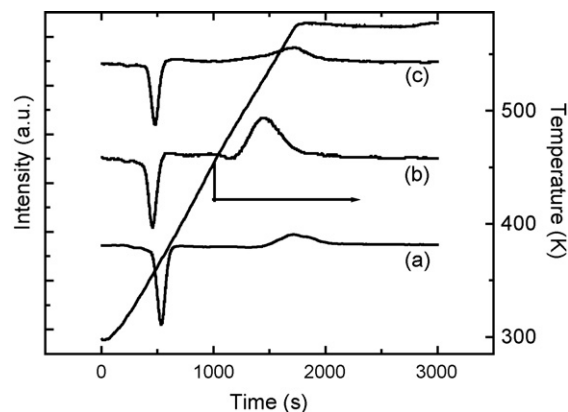

Fig. 6. TPR (to 573 K) profiles for the passivated catalysts (pre-HDC): (a) Pd/SiO$_2$, (b) Sr–Pd/SiO$_2$ and (c) Ba–Pd/SiO$_2$.

certainly demonstrates smaller Pd particle sizes in the bimetallic catalysts and while XRD examination does not support bulk alloy formation, EDX has revealed close proximity of both metals on the surface with possible interactions that limit hydride formation. The TPR of both bimetallics also exhibit a higher temperature H$_2$ consumption that is more intense in the case of Sr–Pd/SiO$_2$. These peaks may be the result of a Pd mediated reduction of the Sr or Ba precursor, which occurs at a lower temperature when compared with Sr/SiO$_2$ or Ba/SiO$_2$, i.e. in the absence of Pd. A similar effect has been demonstrated by Shekar et al. [19].

3.1.3. H$_2$-Chemisorption/TPD

The H$_2$ chemisorptive uptakes recorded subsequent to TPR are given in Table 3a. It must be noted that the chemisorption measurements were conducted under conditions where Pd hydride

Table 3a
BET surface areas, TPR T_{max} and associated H/Pd mol ratios corresponding to Pd hydride decomposition (T_{max} given in bold), H$_2$ uptake and corresponding H$_2$ release (where T = 500–750 K) for the catalysts "pre-HDC"

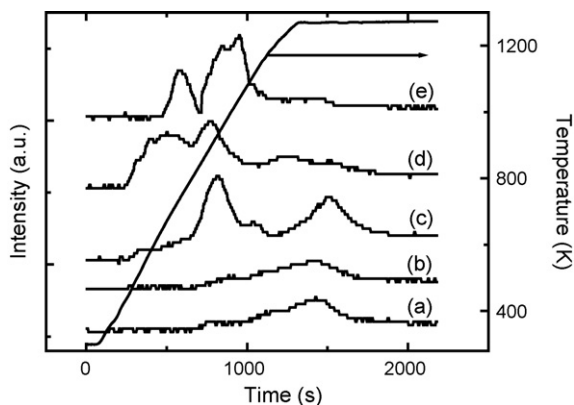| Catalyst	BET area (m^2 g^{-1})	TPR T_{max} (K)	H/Pd	H$_2$ uptake (μmol g^{-1})	H$_2$ release (μmol g^{-1})
Pd/SiO$_2$	191	**371**, 573	0.34	7	6
Sr–Pd/SiO$_2$	143	**366**, 530	0.19	47	43
Ba–Pd/SiO$_2$	154	**369**, 565	0.19	46	44

Fig. 7. TPD (to 1273 K) profiles following H$_2$ chemisorption on the activated catalysts (pre-HDC): (a) Sr/SiO$_2$, (b) Ba/SiO$_2$, (c) Pd/SiO$_2$, (d) Sr–Pd/SiO$_2$, and (e) Ba–Pd/SiO$_2$.

formation was circumvented; see Section 2.1. Uptake on Sr–Pd/SiO$_2$ and Ba–Pd/SiO$_2$ were equivalent and seven times greater than that exhibited by Pd/SiO$_2$; there was no detectable uptake on Sr/SiO$_2$ or Ba/SiO$_2$. The enhancement in uptake due to the presence of AEM is consistent with an increase in Pd dispersion, as confirmed by TEM and XRD (see (Table 1a)). The H$_2$ TPD (up to 1273 K) profiles are presented in Fig. 7 with pertinent H$_2$ release values given in Table 3a. The profiles for Sr/SiO$_2$ and Ba/SiO$_2$ reveal a broad release of H$_2$ that extends into the final isothermal hold (1273 K). This response is similar to that observed earlier for Yb/SiO$_2$ prepared in analogous manner (Yb introduction as a liquid NH$_3$ solution) which we identified [13,56,57] as a composite release with contributions due to amide (precursor) decomposition, SiO$_2$ dehydroxylation and possible hydrogen release from supported hydride. In terms of the Pd based samples, each desorption profile is featureless at $T < 400$ K and the absence of a H$_2$ release peak at 360–370 K due to Pd hydride decomposition, observed during TPR (see Fig. 6), is consistent with an exclusive H$_2$ chemisorption during pulse titration, i.e. no Pd hydride formation. The TPD profile for Pd/SiO$_2$ exhibits three regions of desorption with associated T_{max} values at ca. 600 K (low intensity peak), 900 K and 1273 K (isothermal hold). Taking an overview of the pertinent published studies, the lower T release can be ascribed to a desorption of chemisorbed hydrogen [46,51,58]. In support of such an assertion, it should be noted that the H$_2$ released over the T range (500–750 K) essentially matched that taken up in the chemisorption step which preceded TPD; see entries in Table 3a. Higher temperature H$_2$ release from supported metal systems has typically been attributed to a desorption of spillover hydrogen [46,59–61]. Spillover H$_2$ results from a combined chemisorption on Pd and transport to the SiO$_2$ support during TPR where spillover species associated with the metal/support interface and the support can demonstrate quite different thermal desorption behaviour [61]. Both bimetallics exhibit more intense lower T peaks consistent with desorption of greater amounts of H$_2$ (Table 3a) that correlate reasonably well with the observed enhanced H$_2$ uptake. There is a clear deviation in the subsequent H$_2$ desorption characteristics when compared with Pd/SiO$_2$, a response that can result from AEM/surface interactions that impact on spillover release. While we have no direct evidence for AEM hydride formation, our results indicate that the incorporation of AEM in the bimetallic modifies H$_2$ uptake/release characteristics.

3.1.4. HDC/hydrogenation performance

The catalysts were employed to promote the HDC of CB and 1,2-DCB where the former generated benzene as the primary product while the latter also yielded CB as intermediate. Trace amounts of
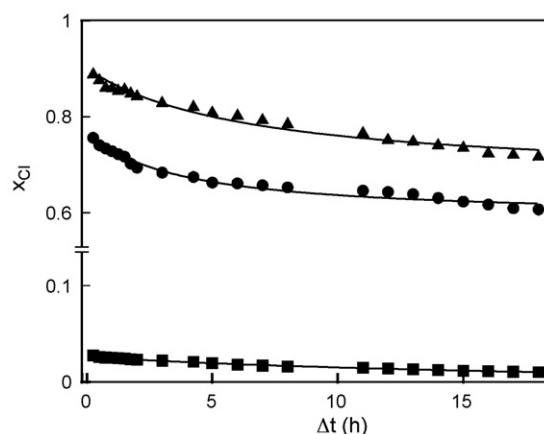

Fig. 8. Fractional dechlorination (x_{Cl}) of CB as a function of time-on-stream: Pd/SiO$_2$ (■); Sr–Pd/SiO$_2$ (●); Ba–Pd/SiO$_2$ (▲).

cyclohexane (<0.1% mol/mol) were also formed in both cases. In every instance, there was a temporal drop in the level of HDC that can be expressed in terms of the empirical relationship

$$\frac{(x_{Cl} - x_0)}{(x_{18\,h} - x_0)} = \frac{\Delta t}{(\beta + \Delta t)} \qquad (5)$$

Fit convergence yields values for x_0, the initial fractional HDC, where x_{18h} represents the fractional conversion after 18 h and β is a time scale fitting parameter. The temporal profiles for CB and 1,2-DCB HDC are shown in Figs. 8 and 9, respectively. HDC over Sr/SiO$_2$ and Ba/SiO$_2$ did not result in any measurable conversion. However, both bimetallic catalysts delivered initial fractional CB dechlorination values that were over an order of magnitude higher when compared with Pd/SiO$_2$ with close to two orders of magnitude enhancement in the case of 1,2-DCB; see entries in Table 4. Under identical reaction conditions, HDC of CB exceeded that of DCB over Pd/SiO$_2$ as a result of combined steric and inductive effects, the latter due to a destabilization of the carbocation (arenium ion) intermediate through the electron withdrawal action of the second Cl substituent, as has been discussed in detail elsewhere [37,62]. It is significant that the difference in chloroarene reactivity is not as pronounced over the bimetallic catalysts, which must be considered a feature of an intrinsic high HDC efficiency. Nevertheless, each catalyst exhibited a time-on-stream decline in conversion, a response that has been observed previously in HDC applications [63]. The ratio of initial to final fractional HDC (x_0/x_{18h}) was significantly
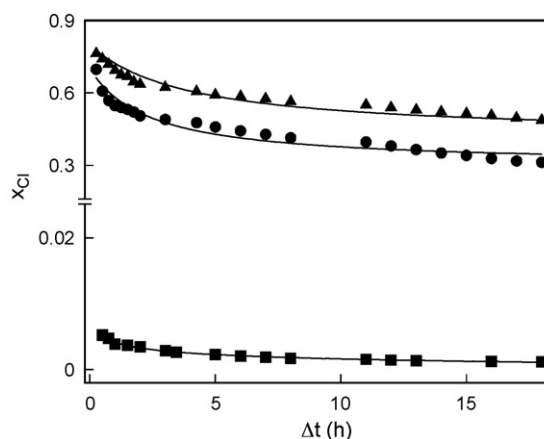

Fig. 9. Fractional dechlorination (x_{Cl}) of 1,2-DCB as a function of time-on-stream: Pd/SiO$_2$ (■), Sr–Pd/SiO$_2$ (●), Ba–Pd/SiO$_2$ (▲).
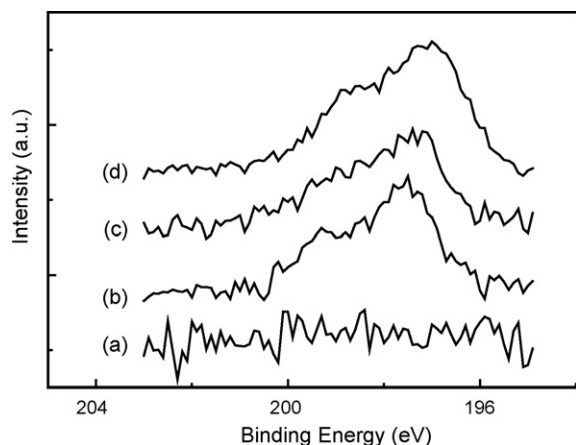
Fig. 10. XPS profiles over the Cl 2p region: (a) Pd/SiO$_2$ (post-HDC), (b) Sr–Pd/SiO$_2$ (post-HDC), (c) Ba–Pd/SiO$_2$ (post-HDC), (d) PdCl$_2$ + SiO$_2$ physical mixture.

Fig. 11. XRD patterns for the catalysts post-HDC: (a) Pd/SiO$_2$, (b) Sr–Pd/SiO$_2$, (c) Ba–Pd/SiO$_2$. *Note*: **O** indicates peak assignment for *fcc* Pd, **X** for SrCl$_2$ and ■ for BaCl$_2$ phases.

lower for both Sr–Pd/SiO$_2$ and Ba–Pd/SiO$_2$, demonstrating that the bimetallics were not only far more active but also less susceptible to deactivation, retaining a higher fractional HDC with time. The enhanced HDC performance due to the inclusion of the AEM component is also apparent from the selectivity behaviour (see Table 4) in the conversion of 1,2-DCB where the bimetallics delivered a much lower S_{CB}, i.e. complete HDC was preferred. A common increase in the time-on-stream S_{CB} was observed for the three catalysts as the activity loss resulted in an increasing involvement of sequential HDC.

The consensus that is emerging from the pertinent literature [63,64] is that catalytic HDC is structure sensitive with some evidence of a metal particle size effect in that larger particles are adjudged to be more active. This trend does not appear to apply in this system as the Sr–Pd/SiO$_2$ and Ba–Pd/SiO$_2$ samples which bear the smallest Pd particles are far more active than Pd/SiO$_2$ (at a common Pd loading) as demonstrated by the initial specific HDC rates (r_0) given in Table 4. The source of enhanced HDC performance must be the result of a critical surface Pd/AEM interplay. The XPS results have demonstrated electron transfer from Sr and Ba to Pd which can have a promotional effect in generating electron rich Pd species that are more effective in activating C–Cl bond(s) for hydrogen scission [29]. It is significant that, in the conversion of both CB and 1,2-DCB, Ba proved (see Figs. 8 and 9 and Table 4) more effective as a promoter compared with Sr. The reason for this is not immediately apparent on the basis of possible electron donation, i.e. similar shift in Pd 3d$_{5/2}$ binding energies for both AEM-Pd/SiO$_2$ samples, or Pd diameter, i.e. similar particle size on the basis of H$_2$ uptake and TEM/XRD analysis. It is however significant that, in marked contrast to Pd/SiO$_2$, both bimetallics post-HDC exhibited the presence of significant residual surface Cl, as confirmed from XPS analysis of the used samples. The XPS profiles are presented in Fig. 10 and binding energy/compositions are included in Table 2. The higher HDC activities delivered by Ba-Pd/SiO$_2$ may de due to a more effective C–Cl bond activation *via* electron donation, which is consistent with the lower Pauling electronegativity value for Ba (0.89) compared with Sr (0.95) [65]. Such an effect finds indirect support in the post-HDC XPS analysis where Ba-Pd/SiO$_2$ bore a measurably higher Cl content, presented in Table 2 as a Cl/(AEM + Pd) atom ratio. Evidence for strong Cl/AEM interaction(s) is also provided from XRD analysis, as shown in Fig. 11. The diffractograms for the used bimetallics include peaks corresponding to SrCl$_2$ and BaCl$_2$ in addition to cubic Pd but there was no detectable bulk PdCl$_2$ formation. TEM-EDX analysis also revealed the presence of residual Cl post-HDC; a representative TEM image for Sr–Pd/SiO$_2$ is given in Fig. 12 with the
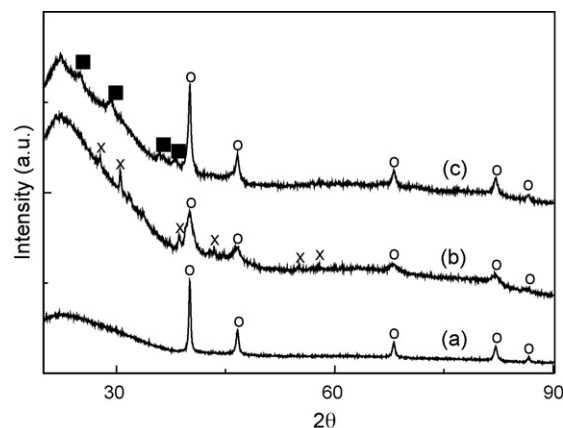
elemental compositions of the mapped areas included in Table 1b. Moreover, the TPR (not shown) of the passivated used bimetallics included a H$_2$ consumption at ca. 430 K (see Table 3b) that was not present in the TPR of the spent Pd/SiO$_2$ sample and which can be attributed to a dehydrochlorination of the surface. Indeed, passage of the effluent gas during TPR of the used bimetallics through an aqueous NaOH trap (3.5–8.0 × 10^{-3} mol dm^{-3}, agitation at 400 rpm with continuous pH data logging [66]) revealed a drop in pH that is consistent with HCl release.

While the BET areas were not significantly altered post-reaction, H$_2$ uptake (and associated release during TPD) was appreciably lower on the used samples (Table 3b). This effect has been observed elsewhere and ascribed to a Cl induced poisoning [67,68]. The Pd hydride composition in the used samples differed from that recorded pre-HDC, particularly in the case of Pd/SiO$_2$ (Table 3b). The latter can be accounted for by Pd particle growth [50] which is consistent with the TEM/XRD measurements given in Table 1a. Metal sintering of supported Pd catalysts during HDC operation
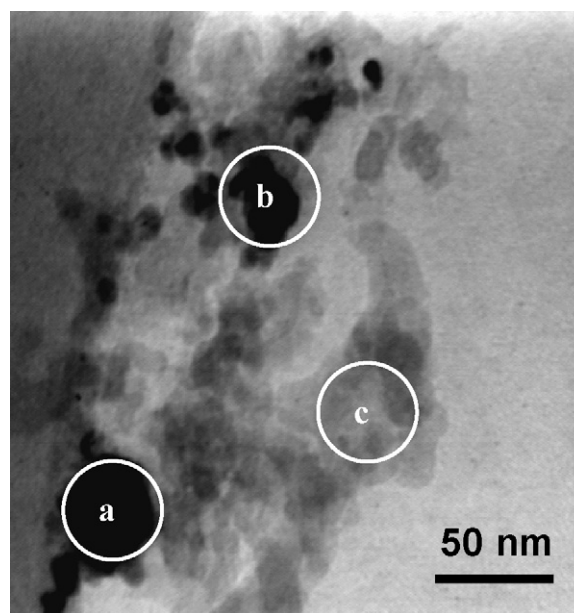

Fig. 12. Representative TEM image of Sr–Pd/SiO$_2$ (post-HDC) with three encircled areas that were subjected to EDX analysis: see Table 1b for the resultant elemental composition.

Table 3b

BET surface areas, TPR T_{max} and associated H/Pd mol ratios corresponding to Pd hydride decomposition (T_{max} given in bold), H_2 uptake and corresponding H_2 release (where $T = 500–760$ K) for the catalysts "post-HDC"

Catalyst	BET area ($m^2 g^{-1}$)	TPR T_{max} (K)	H/Pd	H_2 uptake ($\mu mol\, g^{-1}$)	H_2 release ($\mu mol\, g^{-1}$)
Pd/SiO$_2$	184	**374**	0.59	2	<1
Sr–Pd/SiO$_2$	137	**368**, 433	0.26	18	14
Ba–Pd/SiO$_2$	146	**370**, 430	0.26	19	14

Table 4

HDC performance in terms of initial fractional HDC (x_0), ratio of initial fractional HDC to that recorded after 18 on-stream ($x_0/x_{18\,h}$), selectivity to CB (S_{CB}) in the conversion of 1,2-DCB and initial specific HDC rate (r_0, $mol_{Cl}\, h^{-1}\, m^{-2}$)

	Pd/SiO$_2$	Sr–Pd/SiO$_2$	Ba/Pd/SiO$_2$
CB			
x_0	0.04	0.77	0.90
$x_0/x_{18\,h}$	4.5	1.3	1.2
r_0	0.24	0.58	0.85
1,2-DCB			
x_0	0.01	0.72	0.81
$x_0/x_{18\,h}$	5.5	2.2	1.6
$(S_{CB})_0$%	81	4	3
$(S_{CB})_{18\,h}$ %	100	40	34
r_0	0.04	0.57	0.78

has been reported previously in the literature [33,69]. The bimetallic samples exhibited some surface restructuring post-HDC as can be assessed from the XPS profiles included in Figs. 5 and 13. The XPS spectrum over the Pd 3d doublet region for the used Pd/SiO$_2$ (Fig. 13) is indistinguishable from that recorded for the sample pre-HDC (Fig. 5I), characterized by distinct Pd 3d$_{3/2}$ and Pd 3d$_{5/2}$ signals with identical binding energies (Table 2). However, the Pd XPS signal for the used bimetallic catalysts show a marked disruption when compared with the response pre-HDC. A "splitting" of the Pd 3d$_{5/2}$ is apparent for the post-HDC Sr–Pd/SiO$_2$ sample, a feature that is characteristic of the XPS spectrum of PdCl$_2$, which is also included (physical mixture with SiO$_2$) in Fig. 13. Whereas peak splitting is not obvious for the used Ba–Pd/SiO$_2$, the signal is noticeably broadened suggestive of some surface modification. The XPS spectra of Sr 3d$_{5/2}$ and Ba 3d$_{5/2}$ for the post-HDC bimetallic samples are shown in Fig. 5II (profile (c)) and Fig. 5III (profile (c)) and, when compared with the pre-HDC samples, exhibit an increase in binding energy by up to 0.6 eV (see Table 2) which can be accounted for in terms of chloride formation, as confirmed by XRD. TEM analysis has also revealed appreciable surface restructuring, notably a redispersion of the AEM component where the clustering
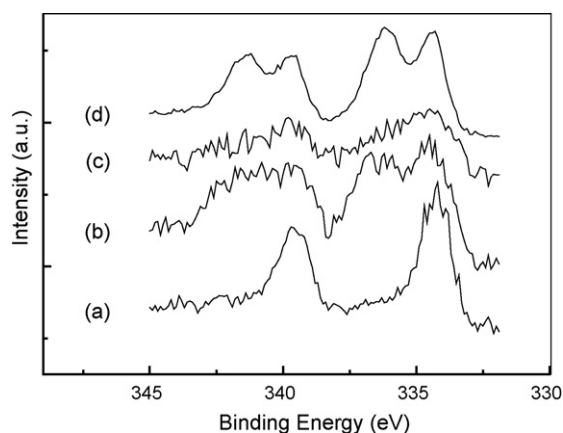
that characterized the samples pre-HDC is no longer a prominent feature (see Fig. 12 and Table 1b). Moreover, the Pd component exhibited a broader size range (with particles of up to 40 nm diameter detected) with a resultant larger mean size that also emerges from the XRD measurement (Table 1a). It is also significant that the appreciable Cl content associated with used Ba–Pd/SiO$_2$ resulted in a surface enrichment by Ba while the Sr/Pd atom ratio remained largely unchanged (Table 2).

In order to probe the role of AEM additives in hydrogen mediated reactions further, we examined the hydrogenation of benzene over the three catalysts pre- and post-(1,2-DCB) HDC. The results are presented in Fig. 14 where cyclohexane was the only detected product. The literature on AEM effects in benzene hydrogenation is limited but Castillon et al. [70] have observed no change in activity resulting from the introduction of Ba to Ni/SiO$_2$ whereas Ca incorporation served to inhibit benzene hydrogenation, a response that was linked to a Ni particle size (increased in the presence of Ca) effect. Li and Shao [71], in studying the hydrogenation of benzene, dehydrogenation of cyclohexane and isomerization of *n*-hexane over AEM (Mg, Ca, Sr and Ba) doped Pt/β-zeolite found that the highest activity resulted from Ba addition and ascribed this to modifications to surface acidity. Fujie et al. [72] reported an increase in benzene (and toluene) hydrogenation performance with the introduction of BaO to Ni/Al$_2$O$_3$ that was directly proportional to the accompanying increase in H$_2$ chemisorption, a result that was taken to be diagnostic of structure insensitivity. Imamura et al. [73] found that Sr/SiO$_2$ and Ba/SiO$_2$, prepared in a similar manner to that adopted in this work, exhibited some initial activity (with a subsequent temporal loss) in the partial hydrogenation of benzene to cyclohexene. The AEM/SiO$_2$ samples prepared in this study were found to be inactive. In accordance with Castillon et al. [70], we observed no significant difference in benzene hydrogenation performance due to the presence of AEM, prior to HDC. The enhanced HDC performance associated with the bimetallics (solid bars) is again demonstrated in Fig. 14. Post-HDC, the benzene hydrogenation activity of Pd/SiO$_2$ declined, presumably as a result of Cl poisoning. In stark contrast, cyclohexane yield over the

Fig. 13. XPS profiles over the Pd 3d doublet region: (a) Pd/SiO$_2$ (post-HDC), (b) Sr–Pd/SiO$_2$ (post-HDC), (c) Ba–Pd/SiO$_2$ (post-HDC), (d) PdCl$_2$ +SiO$_2$ physical mixture.
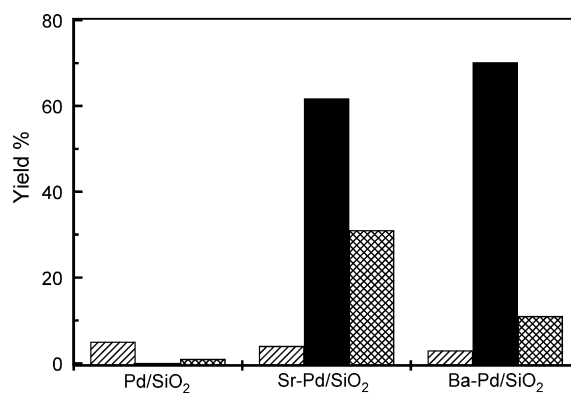

Fig. 14. Steady state cyclohexane yield from benzene hydrogenation over freshly activated catalysts (hatched bars), benzene yield from 1,2-DCB HDC (solid bars) and cyclohexane yield from benzene hydrogenation post-HDC (cross-hatched bars): see Section 2.2 for reaction conditions.

bimetallics post-HDC was increased by a factor of 8 and 4 in the case of Sr–Pd/SiO$_2$ and Ba–Pd/SiO$_2$, respectively. This enhancement must be linked to the surface modifications that result from the intermediate HDC treatment, i.e. redispersion of both the Pd and AEM component and (possibly) the incorporation of surface Cl. At this juncture we can only flag possible effects but this unexpected enhancement of benzene hydrogenation over "HDC deactivated" bimetallics will be the topic for a future detailed study.

4. Conclusions

In the gas phase HDC of CB or 1,2-DCB, Sr–Pd/SiO$_2$ and Ba–Pd/SiO$_2$ significantly outperformed Pd/SiO$_2$ in terms of specific HDC rate (increase by a factor of up to 20) and durability; Sr/SiO$_2$ or Ba/SiO$_2$ exhibited no measurable HDC activity. The AEM/Pd bimetallics were prepared in one step from the organometallic precursor $\{(DMF)_x AEMPd(CN)_4\}_\infty$, the first time such a complex has been used for supported Pd/AEM catalyst preparation. BET measurements of the AEM containing catalysts revealed a loss of surface area that can be attributed to a partial pore filling. The molar H/Pd ratio associated with Pd hydride was lower in the case of the bimetallics suggesting some inhibition of hydride formation while H$_2$ chemisorptive uptake was elevated as a result of AEM inclusion. The latter effect can be linked, at least in part, to an enhanced Pd dispersion in AEM-Pd/SiO$_2$ that is demonstrated by TEM and XRD measurements. The freshly activated AEM-Pd/SiO$_2$ catalysts exhibited AEM particles/clusters with diameters up to up to 90 nm (Pd particles <15 nm) and a heterogeneity in terms of AEM/Pd atomic ratios. We attribute the enhanced HDC performance to a more effective C–Cl bond activation in tandem with an increased surface active hydrogen component that is the result of a surface Pd/AEM synergy. Each catalyst suffered a time-on-stream deactivation that can be linked to deleterious Cl/catalyst interactions, which serve to inhibit H$_2$ uptake, induce Pd sintering with a redistribution of surface AEM and a disruption to the electronic character of the supported sites. While the incorporation of AEM had no significant effect on Pd promoted benzene hydrogenation, post-HDC bimetallics delivered a significant increase in cyclohexane yield, a response that we ascribe to a Cl induced surface reconstruction.

Acknowledgements

References

[1] J.K. Fawell, S. Hunt, Environmental Toxicology Organic Pollutants, Ellis Horwood, Chichester, 1988.
[2] USEPA, Toxic Release Inventory, Public Data Release, Office of Pollution Prevention and Toxics, Washington DC, 1991.
[3] J.F. McEldowney, S. McEldowney, Environment and the Law, Longman, Essex, 1996.
[4] J.G. Bryant, in: J.L. Kroschwitz, M. Howe-Grant (Eds.), The Kirk-Othmer Encyclopedia of Chemical Technology, Vol. 6, fourth ed., John Wiley, New York, 1993, pp. 87–100.
[5] F.J. Urbano, J.M. Marinas, J. Mol. Catal. A: Chem. 173 (2001) 329.
[6] V.V. Lunin, E.S. Lokteva, Russ. Chem. Bull. 45 (1996) 1519.
[7] F. Alonso, I.P. Beletskaya, M. Yus, Chem. Rev. 102 (2002) 4009.
[8] H. Sajiki, A. Kume, K. Hattori, K. Hirota, Tetrahedron Lett. 43 (2002) 7247.
[9] Y. Monguchi, A. Kume, K. Hattori, T. Maegawa, H. Sajiki, Tetrahedron 62 (2006) 7926.
[10] G. Yuan, M.A. Keane, J. Catal. 225 (2004) 510.
[11] G. Yuan, M.A. Keane, Appl. Catal. B: Environ. 52 (2004) 301.
[12] S. Jujjuri, E. Ding, S.G. Shore, M.A. Keane, Appl. Organomet. Chem. 17 (2003) 493.
[13] S. Jujjuri, E. Ding, E. Hommel, S.G. Shore, M.A. Keane, J. Catal. 239 (2006) 486.
[14] S. Jujjuri, E. Ding, S.G. Shore, M.A. Keane, J. Mol. Catal. A: Chem. 227 (2007) 96.
[15] L. Wright, S. Weller, J. Am. Chem. Soc. 76 (1954) 5302 (ibid., 5305; ibid., 5948).
[16] N. Koizumi, K. Murai, S. Tamayama, T. Ozaki, M. Yamada, Energy Fuels 17 (2003) 829.
[17] A. Gotti, R. Prins, J. Catal. 175 (1998) 302.
[18] V.I. Simagina, V.V. Litvak, I.V. Stoyanova, V.A. Yakovlev, V.M. Mastekhin, I.V. Afanesenkova, V.A. Likholobov, Russ. Chem. Bull. 46 (1996) 1321.
[19] S.C. Shekar, J.K. Murthy, P.K. Rao, K.S.R. Rao, E. Kemnitz, Appl. Catal. A: General 244 (2003) 39.
[20] E. Lopez, S. Ordonez, H. Sastre, F.V. Diez, J. Hazard. Mater. 97 (2003) 281.
[21] B. Coq, G. Ferrat, F. Figueras, J. Catal. 101 (1986) 434.
[22] P. Bodnariuk, B. Coq, G. Ferrat, F. Figueras, J. Catal. 116 (1989) 459.
[23] N. Lingaiah, P.S.S. Prasad, P.K. Rao, L.E. Smart, F.J. Berry, Appl. Catal. A: General 213 (2001) 189.
[24] J.L. Benitez, G. Angel, React. Kinet. Catal. Lett. 70 (2000) 67.
[25] M.A. Aramendia, V. Borau, I.M. Garcia, C. Jimenez, F. Lafont, A. Marinas, J.M. Marinas, F.J. Urbano, J. Catal. 187 (1999) 392.
[26] M.A. Aramendia, V. Borau, I.M. Garcia, C. Jimenez, F. Lafont, A. Marinas, J.M. Marinas, F.J. Urbano, J. Mol. Catal. A: Chem. 184 (2002) 237.
[27] L.N. Zanaveskin, V.A. Aver'yanov, Yu.A. Treger, Russ. Chem. Rev. 65 (1996) 617.
[28] A.Yu. Stakheev, L.M. Kustov, Appl. Catal. A: General 188 (1999) 3.
[29] B. Coq, F. Figueras, J. Mol. Catal. A: Chem. 173 (2001) 117.
[30] V. Vishwanathan, N. Mahata, M.A. Keane, React. Kinet. Catal. Lett. 72 (2001) 297.
[31] D.W. Knoeppel, J. Liu, E.A. Meyers, S.G. Shore, Inorg. Chem. 37 (1998) 4828.
[32] S.G. Shore, E. Ding, C. Park, M.A. Keane, Catal. Commun. 3 (2002) 77.
[33] A. Gampine, D.P. Eyman, J. Catal. 179 (1998) 315.
[34] K.V. Murthy, P.M. Patterson, G. Jacobs, B.H. Davis, M.A. Keane, J. Catal. 223 (2004) 74.
[35] K.V. Murthy, P.M. Patterson, M.A. Keane, J. Mol. Catal. A: Chem. 225 (2005) 149.
[36] G. Tavoularis, M.A. Keane, J. Chem. Technol. Biotechnol. 74 (1999) 60.
[37] C. Menini, C. Park, E.-J. Shin, G. Tavoularis, M.A. Keane, Catal. Today 62 (2000) 355.
[38] S.G. Shore, E. Ding, C. Park, M.A. Keane, J. Mol. Catal. A: Chem. 212 (2004) 291.
[39] JCPDS-ICDD, PCPDFWIN, Version 2.2, June 2001.
[40] V.N. Fokin, E.E. Fokina, S.P. Shilkin, Zh. Obsh. Khim. 66 (1996) 1249.
[41] V.N. Fokin, S.L. Troitskaya, E.E. Fokina, S.P. Shilkin, Zh. Neorg. Khim. 36 (1991) 299.
[42] P.A. Weyrich, H. Treviño, W.F. Hölderich, W.M.H. Sachtler, Appl. Catal. A: General 163 (1997) 31.
[43] X.L. Seoane, N.S. Fígoli, P.C.L. Argentiere, J.A. González, A. Arcoya, Catal. Lett. 47 (1997) 213.
[44] S. Suhonen, M. Valden, M. Pessa, A. Savimäki, M. Härkönen, M. Hietikko, J. Pursiainen, R. Laitinen, Appl. Catal. A: General 207 (2001) 113.
[45] M. Nagoshi, Y. Syono, M. Tachiki, Y. Fukuda, Phys. Rev. B 51 (1995) 9352.
[46] C. Amorim, G. Yuan, P.M. Patterson, M.A. Keane, J. Catal. 234 (2005) 268.
[47] F.B. Noronha, M. Schmal, B. Moraweck, P. Delichère, M. Brun, F. Villain, R. Fréty, J. Phys. Chem. B 104 (2000) 5478.
[48] C.-B. Wang, H.-K. Lin, C.-M. Ho, J. Mol. Catal A: Chem. 180 (2002) 285.
[49] C. Yang, J. Ren, Y. Sun, Catal. Lett. 84 (2002) 123.
[50] N.K. Nag, J. Phys. Chem. B 105 (2001) 5945.
[51] V.H. Sandoval, C.E. Gigola, Appl. Catal. A: General 148 (1996) 81.
[52] L.M. Gomez-Sainero, A. Cortes, X.L. Seoane, A. Arcoya, Ind. Eng. Chem. Res. 39 (2000) 2849.
[53] J. Murthy, S. Shekar, V. Kumar, K. Rao, Catal. Commun. 3 (2002) 145.
[54] F. Pinna, M. Signoretto, G. Strukul, S. Polizzi, N. Pernicone, React. Kinet. Catal. Lett. 60 (1997) 9.
[55] J. Batista, A. Pintar, D. Mandrino, M. Jenko, V. Martin, Appl. Catal. A: General 206 (2001) 113.
[56] A.-G. Boudjahem, S. Monteverdi, M. Mercy, D. Ghanbaja, M.M. Bettahar, Catal. Lett. 84 (2002) 115.
[57] V.I. Bogillo, L.S. Pirnach, A. Dabrowski, Langmuir 13 (1997) 928.
[58] J.H. Sepúlveda, N.S. Fígoli, Appl. Surf. Sci. 68 (1993) 257.
[59] F. Benseradj, F. Sadi, M. Chater, Appl. Catal. A: General 228 (2002) 135.
[60] E.-J. Shin, A. Spiller, G. Tavoularis, M.A. Keane, Phys. Chem. Chem. Phys. 1 (1999) 3173.
[61] W.C. Conner Jr., J.L. Falconer, Chem. Rev. 95 (1995) 759.
[62] E.-J. Shin, M.A. Keane, Appl. Catal. B: Environ. 18 (1998) 241.
[63] R. Gopinath, K.N. Rao, P.S.S. Prasad, S.S. Madhavendra, S. Narayanan, G. Vivekanandan, J. Mol. Catal. A: Chem. 181 (2002) 215.
[64] W. Juszczyk, A. Malinowski, Z. Karpiński, Appl. Catal. A: General 166 (1998) 311.
[65] C.H. Suresh, N. Koga, J. Am. Chem. Soc. 124 (2002) 1790.
[66] G. Yuan, M.A. Keane, Chem. Eng. Sci. 58 (2003) 257.
[67] G. Yuan, M.A. Keane, Catal. Today 88 (2003) 27.
[68] D.J. Moon, M.J. Chung, K.Y. Park, S.I. Hong, Appl. Catal. A: General 168 (1998) 159.
[69] D.A. Dodson, H.F. Rase, Ind. Eng. Chem. Prod. Res. Dev. 17 (1978) 236.
[70] F.F. Castillon, N. Bodganchikova, S. Fuentes, M. Avalos-Borja, Appl. Catal. A: General 175 (1998) 55.
[71] G. Li, Y. Shao, Fushun Shiyou Xueyuan Xuebao 20 (2000) 22.
[72] H. Fujie, K. Mori, K. Tamura, S. Okada, S. Matsuoka, H. Matsuoka, Chem. Lett. 9 (1982) 1449.
[73] H. Imamura, K. Mizuno, K. Ohishi, E. Suda, K. Kanda, Y. Sakata, S. Tsuchiya, J. Alloys Compd. 275–277 (1998) 903.